Contents

1. Surface relaxation theory

Molecular liquids imbibed within mesoporous solids can experience significant adsorption interactions with the pore walls, as well as bulk-like behaviour towards the centre of the pores. The rate of mixing between these environments can have notable effects on the observed NMR relaxation characteristics of the imbibed liquid. For small, non-viscous molecules, it is typical for exchange between surface and bulk environments to be significantly more rapid than the rates of nuclear spin relaxation being measured.[1] This condition is described by the fast diffusion limit,[2]

$$\frac{\rho_2 \ell_s}{\mathcal{D}_0} \ll 1, \tag{S 1}$$

where $\rho_2 \equiv \delta/T_{2,surf}$ is the transverse surface relaxivity, ℓ_s is a characteristic length scale defining the pore size and $\mathcal{D}_0$ is the bulk liquid self-diffusion coefficient. Provided Equation (S 1) is valid for the system under study we may assume the presence of fast, biphasic molecular exchange between an adsorbed surface layer of thickness δ and bulk-like liquid towards the centre of the pores. The observed relaxation rates $1/T_{i,obs}$ are therefore a weighted average of bulk and surface contributions, described by

$$\frac{1}{T_{i,obs}} = \frac{1-P}{T_{i,bulk}} + \frac{P}{T_{i,surf}}. \tag{S 2}$$

Here, $i = 1{,}2$ indicates longitudinal or transverse nuclear spin relaxation and $P = \delta S/V$ is the proportion of spins (molecules) within the adsorbed surface layer, where S/V is the surface-to-volume ratio of the material under study. $T_{i,bulk}$ and $T_{i,surf}$ are the nuclear spin relaxation time constants within the bulk and adsorbed surface layer, respectively. Such a description is particularly valid for wetting liquids confined to mesopores with weakly relaxing surfaces,[1] and has also been shown to be applicable to cyclohexane in silica nanopores.[3] Equation (S 2) is therefore appropriate for the liquid-saturated silica investigated in this work.

As liquid-phase nuclear spin relaxation is dominated by the modulation of local dipole-dipole interactions occurring at the Larmor frequency, the relaxation rates of species within the adsorbed surface layer are readily perturbed by the presence of solid-liquid interfaces due to a reduction in the translational and rotational mobility of molecules upon adsorption.[4–6] Such interfaces are of course common within mesoporous media saturated with molecular liquids. As a result, adsorbed species experience enhanced relaxation rates relative to the bulk, such that $T_{i,surf} \ll T_{i,bulk}$. Provided that the S/V of the material under study is sufficiently large we find that

$$\frac{1}{T_{i,obs}} \approx \frac{\delta S}{V}\frac{1}{T_{i,surf}}, \tag{S 3}$$

such that the observed relaxation rates are considered inherently surface sensitive. Importantly, $T_{1,obs}/T_{2,obs}$ values are – to leading order – now independent of the S/V and δ components of Equation (S 2). As the ratio $T_{1,surf}/T_{2,surf}$ is considered a measure of surface affinity,[7] this approximation allows the comparison of surface interactions strengths across porous media with different pore size characteristics, or as discussed in the present work, when saturated with different liquids.

2. Supplementary experimental methods

2.1. Bulk-liquid T_1 measurements

Longitudinal bulk liquid relaxation time constants, $T_{1,bulk}$, were measured using a Bruker Biospin horizontal bore magnet as described in the main text. The time-dependent recovery of longitudinal nuclear spin relaxation was measured using the standard inversion recovery technique,[8] as illustrated in Figure S1. All experiments were performed at room temperature and under ambient pressure. 16 τ_1 recovery times were employed ranging from 1 ms – 20 s. The acquired data were then fit to

$$\frac{S(t)}{S_0} = 1 - 2\exp\left\{\frac{-t}{T_1}\right\} \quad \text{(S 4)}$$

in order to extract $T_{1,bulk}$ for each liquid. Here, $S(t)$ is the time-dependent NMR signal associated with longitudinal magnetisation and S_0 is the signal acquired at equilibrium magnetisation. Only the alkyl peaks of each alcohol were analysed and compared in the present work.

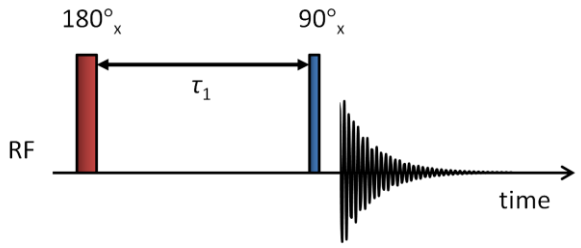

Figure S1. Pulse sequence diagram for the inversion recovery experiment, illustrating the longitudinal recovery delay τ_1. Red and blue vertical bars represent $180°$ and $90°$ radiofrequency (RF) pulses, respectively.

2.2. Bulk-liquid PFG NMR diffusion measurements

Pulsed-field gradient (PFG) NMR diffusion measurements were performed using a Bruker DMX spectrometer equipped with a 7.1 T magnet (300.13 MHz for ^{1}H) and a Bruker Biospin Diff-30 diffusion probe capable of generating magnetic field gradient pluses up to 11.76 T m^{-1}. The diffusion of pure bulk liquids was analysed using the pulsed gradient stimulated echo (PGSTE) sequence as shown in Figure S2. Self-diffusion coefficients, $\mathcal{D}_0$, were calculated by fitting the acquired experimental data to the Stejskal-Tanner equation,[9]

$$\frac{S(g)}{S_0} = \exp\left\{-\mathcal{D}_0\gamma^2 g^2 t_\delta^2\left(t_\Delta - \frac{t_\delta}{3}\right)\right\}, \quad \text{(S 5)}$$

where S_0 is the NMR signal in the absence and of any applied gradient, $S(g)$ is the NMR signal in the presence of applied gradients of magnitude g and duration t_δ, γ is the gyromagnetic ratio of ^{1}H, and t_Δ is the observation time during which molecules are allowed to diffuse. In the present work, PGSTE measurements were carried out by holding t_δ = 1 ms constant and varying the magnetic field gradient strength; 16 linearly spaced g values were used while the observation time was set to t_Δ = 50 ms. A homospoil gradient of magnitude $g_{max}/3$ and length t_H = 10 ms was applied during the storage interval T to remove any coherent transverse magnetisation, and the echo time was set to τ = 3.2 ms. All measurements were performed at 20 ± 0.1 °C and under ambient pressure.

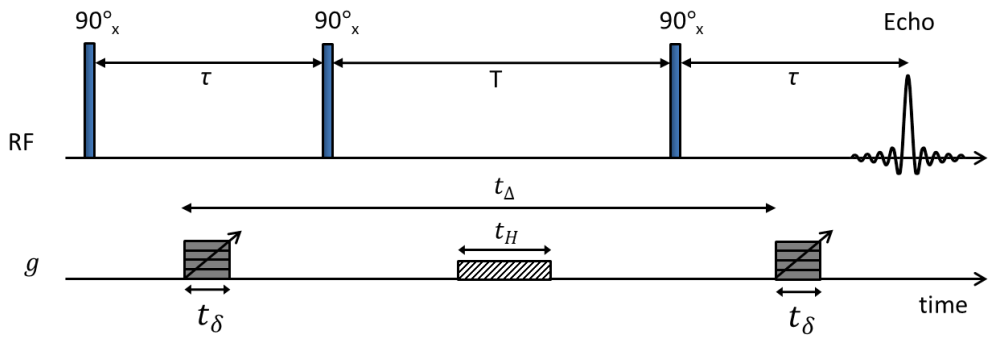

Figure S2. Pulse sequence diagram for the PGSTE diffusion experiment, illustrating gradient pulse duration, t_δ, echo time, τ, storage interval, T, homospoil gradient duration, t_H, and observation time, $t_\Delta = \tau + \mathrm{T}$. Blue vertical bars represent 90° radiofrequency (RF) pulses, while solid grey blocks represent gradient pulses of area $t_g g$. The dashed homospoil gradient has an area of $t_H\, g_{max}/3$.

2.3. Pore size measurements

Nitrogen porosimetry measurements were performed using a Micromeritics TriStar 3000 automated gas adsorption analyser. Specific surface areas (S_{BET}) were obtained by fitting the acquired data to the BET equation, while pore volume (V_{BJH}) and average diameter (d_{BJH}) values were calculated using the BJH method. All nitrogen adsorption measurements were carried out at 77 K.

3. Supplementary experimental results

The $T_1 - T_2$ correlation plot for cyclohexane-saturated silica is depicted in Figure S3. A single correlation peak is observed with $\langle T_1/T_2 \rangle$ = 1.9 ± 0.1, indicating weak adsorption at the pore surface.

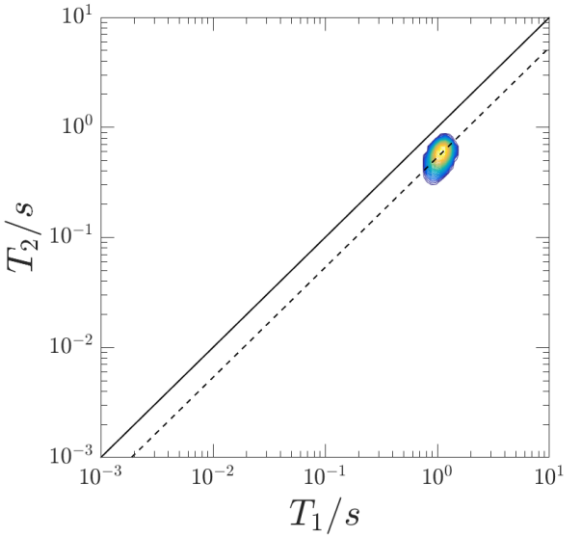

Figure S3. ^{1}H $T_1 - T_2$ correlation plot of cyclohexane-saturated silica. A single correlation peak is observed corresponding to the relaxation of alkyl ^{1}H. The solid diagonal line indicates the parity ratio $T_1 = T_2$. The dashed diagonal line indicates the modal T_1/T_2 ratio, $\langle T_1/T_2 \rangle$, of the correlation peak, with $\langle T_1/T_2 \rangle$ = 1.9 ± 0.1.

1D relaxation time distributions for the liquid/silica systems are provided in Figures S4 – S8, and were obtained through integration of the 2D data shown in Figure S3 and Figure 1 of the main text.

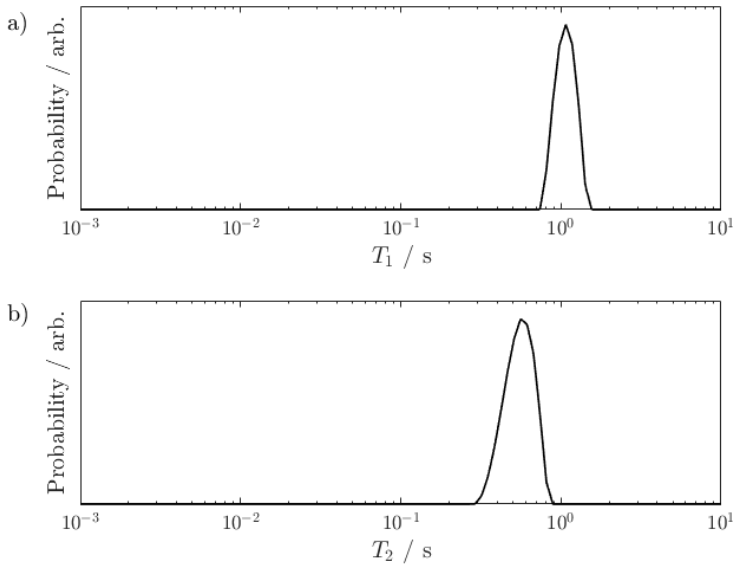

Figure S4. a) T_1 and b) T_2 distributions for cyclohexane in mesoporous silica, obtained through integration of the 2D data presented in Figure S3.

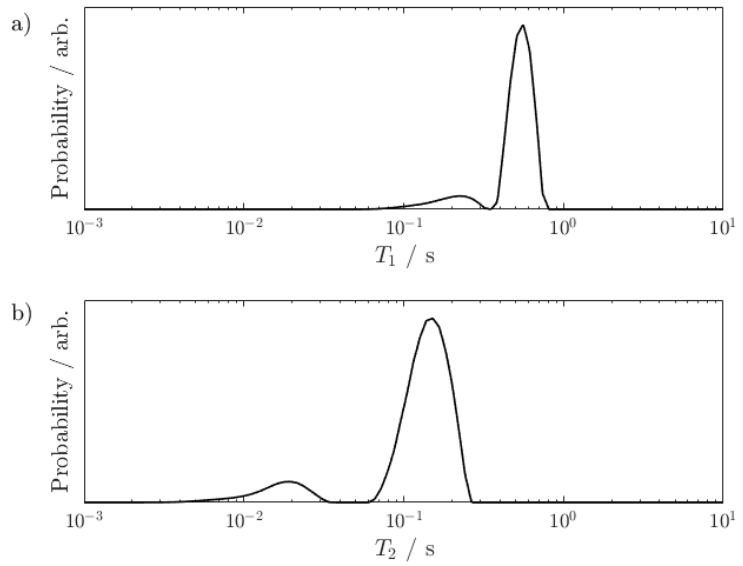

Figure S5. a) T_1 and b) T_2 distributions for methanol in mesoporous silica, obtained through integration of the 2D data presented in Figure 1a of the main text.

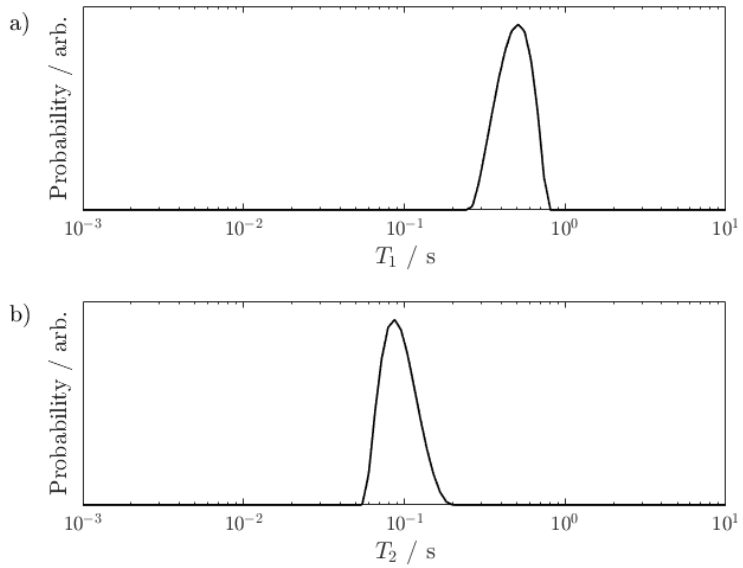

Figure S6. a) T_1 and b) T_2 distributions for ethanol in mesoporous silica, obtained through integration of the 2D data presented in Figure 1b of the main text.

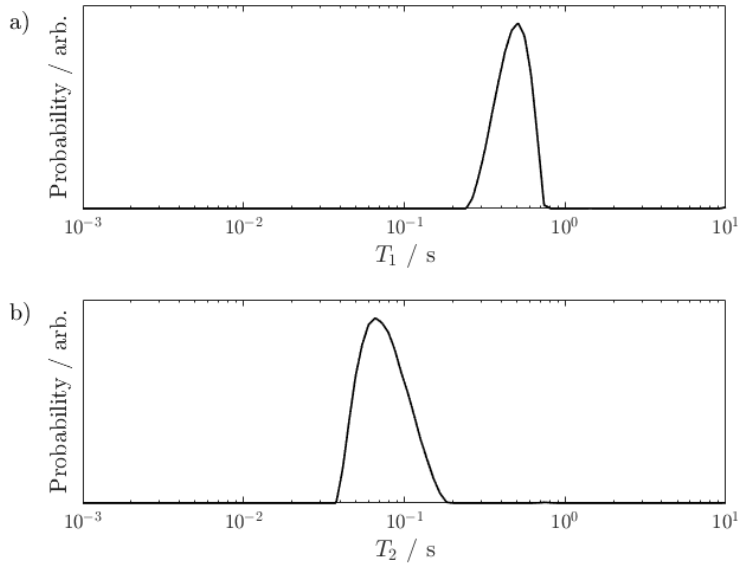

Figure S7. a) T_1 and b) T_2 distributions for 1-propanol in mesoporous silica, obtained through integration of the 2D data presented in Figure 1c of the main text.

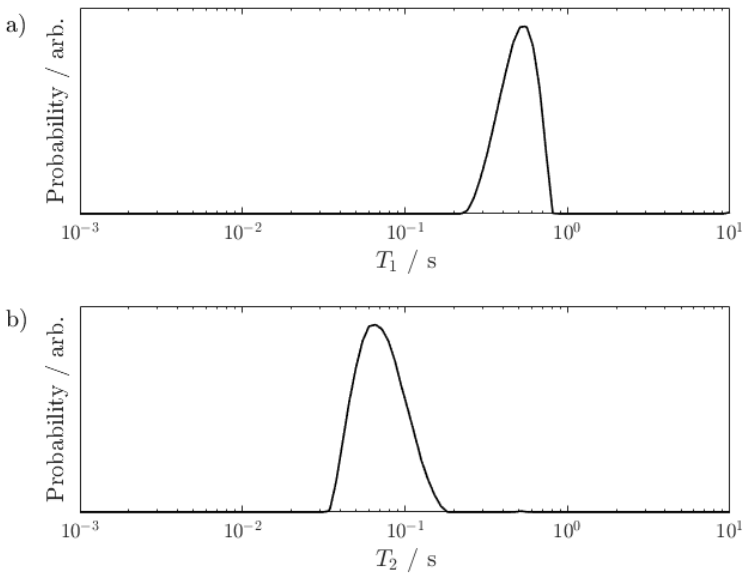

Figure S8. a) T_1 and b) T_2 distributions for 1-butanol in mesoporous silica, obtained through integration of the 2D data presented in Figure 1d of the main text.

Inversion recovery curves for the five bulk liquids investigated are depicted in Figure S9, while log-attenuation plots for the diffusion experiments are shown in Figure S10. The corresponding $T_{1,bulk}$ and $\mathcal{D}_0$ values are summarised in Table S1, along with the $\langle T_1/T_2 \rangle$, $\langle T_1 \rangle$ and $\langle T_2 \rangle$ values obtained from the $T_1 - T_2$ correlation plots described in the main text and in Figure S3.

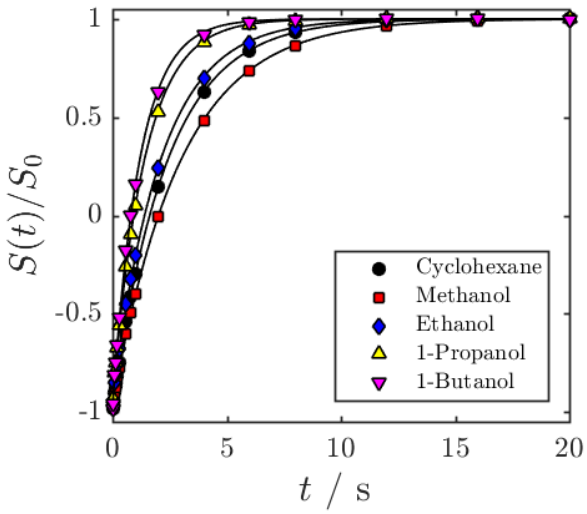

Figure S9. Bulk liquid inversion recovery curves. Solid lines represent fits to the acquired data points using the single exponential function described in Equation (S 4).

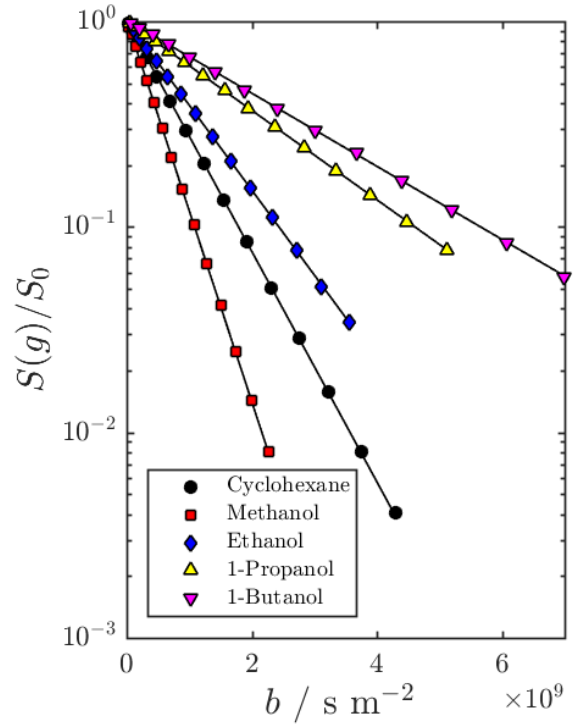

Figure S10. Bulk liquid log-attenuation plots. Solid lines represent fits to the acquired data points using the single exponential function described in Equation (S 5). Note that $b = \gamma^2 g^2 t_\delta^2 \left(t_\Delta - \frac{t_\delta}{3}\right)$.

Table S1. Summary of $T_{1,bulk}$ and $\mathcal{D}_0$ values from the data shown in Figures S9 and S10, along with the modal relaxation time constants and time ratios obtained from the $T_1 - T_2$ correlation experiments described in the main text. All values correspond to the alkyl ^{1}H environment of each molecular liquid.

Molecular Liquid	$T_{1,bulk}$ / s	$\mathcal{D}_0$ × 10^{-10} / m^2 s^{-1}	$\langle T_1/T_2 \rangle$	$\langle T_1 \rangle$ / s	$\langle T_2 \rangle$ / s
Cyclohexane	2.377 ± 0.006	12.91 ± 0.02	1.9 ± 0.1	1.5 ± 0.1	0.56 ± 0.09
Methanol	2.964 ± 0.007	21.40 ± 0.03	3.8 ± 0.3	0.56 ± 0.05	0.15 ± 0.02
Ethanol	2.109 ± 0.005	9.52 ± 0.01	4.9 ± 0.4	0.49 ± 0.05	0.08 ± 0.01
1-Propanol	1.402 ± 0.004	5.01 ± 0.01	6.1 ± 0.5	0.51 ± 0.05	0.07 ± 0.01
1-Butanol	1.177 ± 0.003	4.10 ± 0.01	6.6 ± 0.5	0.51 ± 0.05	0.06 ± 0.01

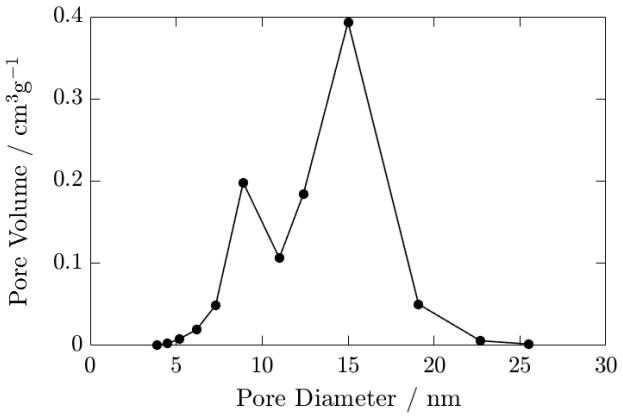

Figure S11. BJH pore size distribution of the mesoporous silica support material.

Table S2. Summary of BET and BJH pore size characteristics for the mesoporous silica used experimentally.

S_{BET} / m^2 g^{-1}	272
V_{BJH} / cm^3 g^{-1}	1.3
d_{BJH} / nm	15
(S_{BET}/V_{BJH}) / m^{-1}	2.1×10^8

4. Supplementary experimental discussion

We now briefly explore the validity of our surface-sensitive interpretation of $\langle T_1/T_2 \rangle$ values, as introduced in Section 1. Two comparisons are performed in order to validate the surface sensitivity of our acquired NMR relaxation data. Firstly, a short discussion of the individual modal time constants $\langle T_1 \rangle$ and $\langle T_2 \rangle$ is presented. Secondly – and more importantly for the results discussed in the present work – a comparison between our acquired $\langle T_1/T_2 \rangle$ values and an estimate of the ratio $T_{1,surf}/T_{2,surf}$ is given.

Key parameters which may be extracted from the fast biphasic molecular exchange model are the surface relaxation time constants $T_{1,surf}$ and $T_{2,surf.}$ Equations (S 2) and (S 3) may be rearranged such that

$$T_{i,surf}(\delta) = P\langle T_i \rangle - \frac{PT_{1,bulk}}{1-P} \tag{S 6}$$

$$\tilde{T}_{i,surf}(\delta) = P\langle T_i \rangle. \tag{S 7}$$

Here, P and $T_{1,bulk}$ maintain their usual meanings and we take $\langle T_i \rangle \equiv T_{i,obs}$. Again, $i = 1{,}2$ indicates longitudinal or transverse nuclear spin relaxation. We also set $T_{1,bulk} \equiv T_{2,bulk}$ which is valid for non-viscous liquids, such that we need only measure the longitudinal relaxation time constant of the bulk liquids; $T_{1,bulk}$ and $\langle T_i \rangle$ values are summarised in Table S1. Surface relaxation time constants $T_{i,surf}(\delta)$ are now dependent on the surface layer thickness δ which is present within the population of adsorbed species P. The value of S/V, which is also present within the term P, is taken from the results of our nitrogen porosimetry measurements in Table S2, such that $S/V \equiv S_{BET}/V_{BHJ}$. Finally, $\tilde{T}_{i,surf}(\delta)$ are the approximate surface relaxation time constants obtained when assuming that the observed relaxation is a result of only surface relaxation and pore structure, as described by Equation (S 3). It is clear from Equations (S 6) and (S 7) that the inherent surface sensitivity of $\langle T_i \rangle$ depends on the relative magnitude of the term $PT_{1,bulk}/(1-P)$.

For the purpose of solving Equations (S 6) and (S 7) we will assume that short-chain primary alcohols at hydroxylated silica surfaces form an adsorbed surface layer with a thickness equivalent to two molecular layers. This assumption is supported by molecular dynamics simulations of methanol at a model silica surface,[10] and experimental observations of ethanol adsorption.[11] We approximate the thickness of an adsorbed monolayer to be equivalent to the kinetic diameter of the molecule of interest d_k, such that $\delta = 2d_k$ for the primary alcohols investigated here; literature d_k values are summarised in Table S3. In the case of cyclohexane we consider the range $\delta = d_k$, $\delta = 2d_k$ and $\delta = 3d_k$.

Table S3 summarises the $T_{i,surf}$ and $\tilde{T}_{i,surf}$ values calculated using Equations (S 6) and (S 7). The results listed here show that $T_{i,surf}$ and $\tilde{T}_{i,surf}$ values are in reasonable agreement with one another, in turn suggesting that Equation (S 3) is a good approximation under the experimental conditions explored in this work. In particular, $T_{2,surf}$ and $\tilde{T}_{2,surf}$ values are found to be in perfect agreement within error, illustrating that the $\langle T_2 \rangle$ values extracted from our $T_1 - T_2$ correlation plots are highly surface sensitive. The small differences between $T_{1,surf}$ and $\tilde{T}_{1,surf}$ suggests that bulk relaxation has a small influence on the observed longitudinal relaxation.

Nevertheless, the two longitudinal surface relaxation time constants exhibit the same trend across the series of liquids examined.

The sensitivity of our extracted modal relaxation time ratios to the adsorbed surface layer is illustrated in Figure S12, where our experimentally obtained $\langle T_1/T_2 \rangle$ values are plotted against the ratio $T_{1,surf}/T_{2,surf}$. A strong, positive correlation is observed, illustrating that $\langle T_1/T_2 \rangle \propto T_{1,surf}/T_{2,surf}$. The value of δ used during our cyclohexane calculations is found to have a negligible influence within the experimental error.

The calculation of $T_{2,surf}$ also allows us to perform a direct evaluation of the fast exchange limit. Each of the liquid-saturated silica samples considered here are found to satisfy Equation (S 1), as quantified in Table S3.

Table S3. Summary of the calculated surface relaxation time constants $T_{i,surf}$ and $\tilde{T}_{i,surf}$ obtained *via* Equations (S 6) and (S 7). Values for the kinetic diameter of each molecule, d_k, are taken from a review by Wu *et al.*[13] and are valid at room temperature. $\rho_2 \ell_s/\mathcal{D}_0$ values have been calculated using the equivalences $\rho_2 \equiv \delta/T_{2,surf}$ and $\ell_s \cong d_{BJH}$.

Molecular liquid	d_k / m	δ	$T_{1,surf}$ / s	$\tilde{T}_{1,surf}$ / s	$T_{2,surf}$ / s	$\tilde{T}_{2,surf}$ / s	$\frac{\rho_2 \ell_s}{\mathcal{D}_0}$
Cyclohexane	6.2×10^{-10}	d_k	0.22 ± 0.02	0.14 ± 0.01	0.09 ± 0.02	0.07 ± 0.01	7.9×10^{-8}
Cyclohexane	6.2×10^{-10}	$2d_k$	0.41 ± 0.04	0.27 ± 0.03	0.18 ± 0.03	0.15 ± 0.02	8.2×10^{-8}
Cyclohexane	6.2×10^{-10}	$3d_k$	0.56 ± 0.05	0.41 ± 0.04	0.26 ± 0.04	0.22 ± 0.04	8.5×10^{-8}
Methanol	3.6×10^{-10}	$2d_k$	0.10 ± 0.01	0.09 ± 0.01	0.023 ± 0.004	0.022 ± 0.004	2.2×10^{-7}
Ethanol	4.5×10^{-10}	$2d_k$	0.12 ± 0.01	0.09 ± 0.01	0.017 ± 0.003	0.016 ± 0.003	8.6×10^{-7}
1-Propanol	4.7×10^{-10}	$2d_k$	0.14 ± 0.01	0.10 ± 0.01	0.014 ± 0.002	0.013 ± 0.002	2.1×10^{-6}
1-Butanol	5.0×10^{-10}	$2d_k$	0.16 ± 0.01	0.11 ± 0.01	0.014 ± 0.002	0.013 ± 0.002	2.6×10^{-6}

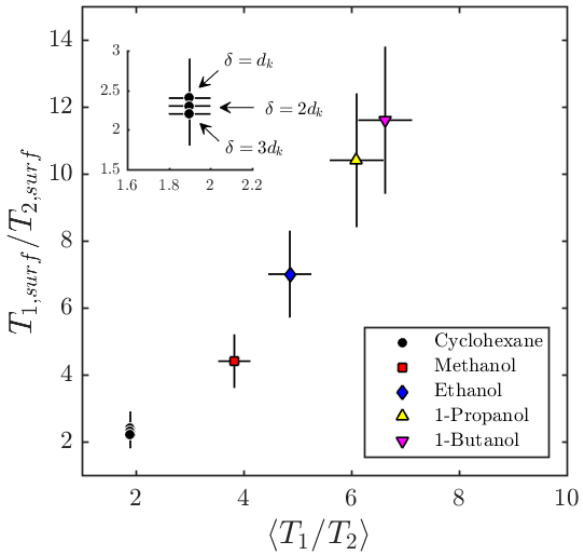

Figure S12. Plot of experimentally observed (alkyl) $\langle T_1/T_2 \rangle$ ratios against $T_{1,surf}/T_{2,surf}$, where $T_{1,surf}$ and $T_{2,surf}$ are defined by Equation (S 6) with values provided in Table S3.

5. Density functional theory calculations

5.1. Methodological approach

Periodic density functional theory (DFT) calculations were performed using the plane wave code CASTEP,[14] utilising the generalised gradient approximation (GGA) level of theory through use of the Perdew-Burke-Ernzerhof (PBE) exchange-correlation functional.[15] All calculations made use of ultrasoft pseudopotentials to represent the core electrons. Dispersion (van der Waals) interactions, which are not explicitly contained within the PBE GGA, were added using the D2 semi-empirical dispersion correction by Grimme (PBE-D2).[16] This correction lies on the first step of the chemical accuracy *vs.* computational cost stairway as described by Klimeš and Michaelides,[17] and provides an excellent compromise between the chemical accuracy of the computed energies and the sizeable computational cost associated with the large number of calculations performed during this work.

5.2. Unit cell optimisation

The α-quartz unit cell was optimised from the experimental values given by Gualtieri (see Table S4).[18] The plane wave basis set was expanded using a 350 eV energy cutoff and reciprocal space was sampled using a 3×3×3 Monkhorst-Pack grid.[19] The geometry optimised unit cell parameters obtained here are given in Table S4 alongside a selection of other parameters obtained through experiments or DFT calculations. We find that our unit cell parameters are in excellent agreement with experimental observations, as is expected considering the excellent performance of the D2 correction in capturing the geometry of bulk crystalline materials.[20]

Table S4. A selection of recent α-quartz unit cell parameters from the literature for comparison against the results reported here. * indicates the experimental parameters used as the initial values for the three unit cell vectors before geometry optimisation.

Exchange-correlation functional / Reference	Experiment		Computational				This work
	Ref [18] *	Ref [21]	PBE[22]	PW91[22]	PW91[23]	PBE[24]	PBE-D2
Unit cell volume /Å^3	113.1994	113.1312	122.6071	123.1112	114.7393	116.4773	113.8779
$\lvert\mathbf{a}\rvert = \lvert\mathbf{b}\rvert$ /Å	4.9158	4.9160	5.0520	5.0560	4.9510	4.9700	4.9284
$\lvert\mathbf{c}\rvert$ /Å	5.4091	5.4054	5.5470	5.5610	5.4050	5.4450	5.4138
Si – O (long) / Å	-	1.614	1.633	1.629	1.626	1.630	1.619
Si – O (short) / Å	-	1.605	1.630	1.632	1.623	1.620	1.614
Si – O – Si / °	-	143.73	147.9	148.6	143.3	142.7	143.01

5.3. Cleavage and hydroxylation of the (0001) α-quartz surface

Utilising the optimised α-quartz unit cell described above, symmetric slabs with a surface area of 1×1 unit cells were cleaved in a number of different thicknesses, i, corresponding to 2 – 5 unit cells. The two symmetric surfaces were designed such that they exhibited the highly reactive Q^2(O) silanone groups (=Si=O), which protrude into the vacuum from undercoordinated surface silicon atoms. These Q^2(O) sites are known to be present upon cleavage of the (0001) surface,[22] and maintain the SiO_2 stoichiometry of the material when cleaved. Slabs were separated in the z-direction by a vacuum gap of 15 Å during each calculation. A method of fixing atoms was also employed such that the uppermost unit cell of each slab along with the upper surface

Q^2(O) site was free to relax, but all other atoms were fixed in place, in order to better represent a pseudo-infinite bulk structure. The 350 eV energy cutoff was maintained for these calculations, with reciprocal space sampled by a 3×3×1 Monkhorst-Pack grid.

Hydroxylated slabs were formed *via* a theoretical dissociative water reaction with these surfaces, such that

$$n\mathrm{O}_{(\mathrm{surf})} + \square + n\mathrm{H_2O}_{(g)} \rightarrow 2n\mathrm{OH}_{(\mathrm{surf})} \qquad \text{(S 8)}$$

where □ represents the vacant 4th coordination site of a surface silicon atom. This surface reaction has been described using Kröger-Vink notation elsewhere.[25] For each 1×1× i slab this requires the addition of one water molecule per surface, where the resulting surfaces exhibit geminal silanol groups ($= \mathrm{Si(OH)_2}$) with a surface silanol density of $\rho_{OH} = 9.51$ nm^{-2}. This value is in perfect agreement with calculations by Musso *et al.*[26] A method of fixing atoms similar to that used for the cleaved surfaces was also employed in order to geometry optimise these surfaces. Here, the upper-most unit cell of each slab, plus the surface hydroxyls from both the top and bottom surfaces were free to relax, but all other atoms were fixed in place. In the following discussion the top-face surface in which both the hydroxyl groups and upper-most unit cell are free to relax will be referred to as the free surface, while the bottom-face surface where only the surface hydroxyl groups remain unfixed will be referred to as the fixed surface. Cleaved and hydroxylated slab are illustrated in Figure S13.

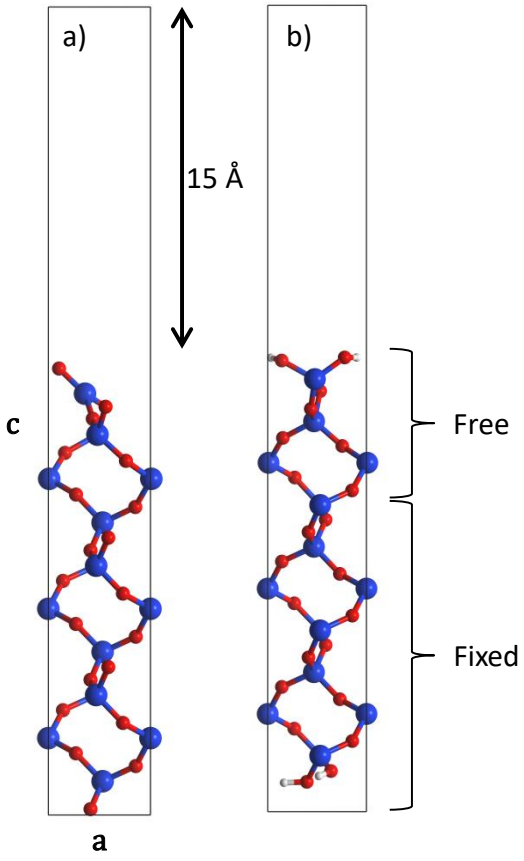

Figure S13. a) The 1x1x3 α-quartz cleaved (0001) surface exhibiting the symmetric surface Q^2(O) sites. b) The 1x1x3 fully hydroxylated α-quartz (0001) surface. Free and fixed regions of the slab are labelled along with 15 Å vacuum gap utilised here. Si, O and H atoms are colour-coded blue, red and white, respectively.

Surface energy calculations were performed on the free hydroxylated surfaces in order to determine the optimum slab thickness for our adsorption energy calculations. The same calculations were also performed on the cleaved surfaces for comparison. Surface energies, γ (in units of J m^{-2}), corresponding to the free surface for each thickness i were calculated according to

$$\gamma = \frac{1}{A}[E_{slab}(i) - \lambda(i)] - \gamma' \quad \text{(S 9)}$$

where A is the surface area of a single slab face and $E_{slab}(i)$ is the geometry optimised slab energy for each slab thickness, i. The term $\lambda(i)$ takes different forms for the cleaved and hydroxylated surfaces. For the cleaved surfaces $\lambda(i) = n(i)E_{bulk}$, where E_{bulk} is the energy of a single α-quartz unit cell and $n(i)$ is a stoichiometric factor such that $n(i) = N_{SiO_2}^{Slab}(i)/N_{SiO_2}^{Bulk}$, and describes the ratio of SiO_2 units within each slab to that within the bulk unit cell. For the hydroxylated surfaces $\lambda(i) = n(i)E_{bulk} + N_{H_2O}E_{H_2O}$ where N_{H_2O} describes the number of water molecules added to each slab ($N_{H_2O} = 2$) and E_{H_2O} is the calculated energy for a single gas phase water molecule. This energy calculation was performed on a single geometry optimised water molecule within a 15×15×15 Å periodic box, where reciprocal space was sampled using only the Γ point. γ' is the surface energy of the fixed surface. This is given by

$$\gamma' = \frac{1}{2A}[E'_{slab}(i) - \lambda(i)] \quad \text{(S 10)}$$

where A and λ maintain their previous definitions and $E'_{slab}(i)$ is the energy of each slab with fixed surfaces. For the cleaved slabs, this corresponds to the singlepoint energy of each slab. For the hydroxylated slabs, this corresponds to the results of a separate geometry optimisation calculation (from the initial, unoptimised configuration) where only the top and bottom face hydroxyls were free to relax (i.e. no slab relaxation was allowed within the uppermost unit cell).

Non-convergence of the calculated γ values with increasing slab thickness[27] were corrected for by the method of Boettger,[28,29] and converged at a thickness of $i = 3$ to $\gamma = -0.17$ J m^{-2} for the hydroxylated surface. This compares to $\gamma = 2.69$ J m^{-2} for the cleaved surface, illustrating the instability of the Q^2(O) surface and suggesting rapid hydroxylation in the presence of water, which is in agreement with previous work on the nature of this reaction.[30] Both sets of surface energies compare well to those calculated by Goumans *et al.* on a similar surface.[22] The $i = 3$ hydroxylated surface was subsequently used in our adsorption energy calculations, and is shown in Figure S13b.

5.4. Methanol adsorption

As introduced in the main text, a methanol probe molecule has been adsorbed across our optimised α-quartz (0001) surface in order to find the most optimal adsorption site for primary alcohols. Methanol was placed approximately 2 Å from the free surface in multiple locations and orientations, and adsorbed through structural relaxation; 8 starting points were sampled across the surface with 4 initial methanol orientations investigated at each location. All calculations involving alcohol adsorbates were performed at a surface

coverage of 1 ML, with the uppermost unit cell of the slab structure free to relax during geometric optimisation as shown in Figure S13. Adsorption energies, E_{ads}, were calculated according to

$$E_{ads} = E_{mol+slab} - (E_{mol} + E_{slab}) \quad \text{(S 11)}$$

where E_{mol} is the energy of the gas phase adsorbate within a 15×15×15 Å periodic box (sampled only at the Γ point), E_{slab} is the energy of the optimised α-quartz slab defined above, and $E_{mol+slab}$ is the energy of the system containing this surface interacting with a single adsorbate. In the present work we consider only the strongest adsorption site found through this sampling. This configuration is shown in Figures 2a and 2b of the main text, and – in agreement with previous work by Han *et al.*[31] – involves multiple surface-adsorbate hydrogen bonding interactions, such that at 1 ML coverage, all surface hydroxyl groups across the α-quartz (0001) surface are active in binding to the adsorbate. This coverage is therefore deemed appropriate for comparison with the liquid-saturated material explored experimentally, where all adsorption site are expected to be saturated.

5.5. Alcohol chain growth

The alcohol chain growth algorithm used here is summarised in Figure S14. The complex structure of the adsorption energy landscape associated with our silica surface (large dependence on initial adsorbate start point, adsorbate orientation and the orientations of surface hydroxyl groups) means that simply attempting to replace the adsorbed methanol with larger molecules is considered a poor method with which to ensure binding of these molecules at the same location. Indeed, due to subtle differences in the optimal surface-adsobate hydrogen bond lengths between different primary alcohols, it was found during our calculations that such an approach typically results in dissociation of the molecule from the surface. In order to mitigate the need to perform our manual adsorption sampling approach for each adsorbate considered, and to ensure the binding of each alcohol at the same location such that adsorption energies might be directly compared across a homologous series of adsorbate alcohols, a different approach utilising a simple chain growth algorithm has been developed. This method uses the initial binding configuration of the adsorbed methanol probe molecule as a 'seed' from which primary alcohols with longer carbon chains may be grown (box 1, Figure S14). Each hydrogen atom within the methyl environment of the adsorbed methanol may be selected (box 2) and separately replaced with an entire methyl group (box 3). This approach yields three adsorbed ethanol molecules which differ only in the orientation of their carbon chain. Structural optimisation (geometric relaxation) of each adsorbate configuration (box 4) is followed by an adsorption energy calculation of the form indicated by Equation (S 11), from which we take the most stable (most negative E_{ads}) configuration as our optimised adsorbate (box 5). The above steps may then be repeated indefinitely to produce larger molecules bound to the same adsorption site. Of course, the fundamental assumption here is that following structural optimisation, the selected configuration is deemed to be acceptably close to the global minimum within an adsorption energy landscape describing the interaction of each adsorbate with the α-quartz (0001) surface.

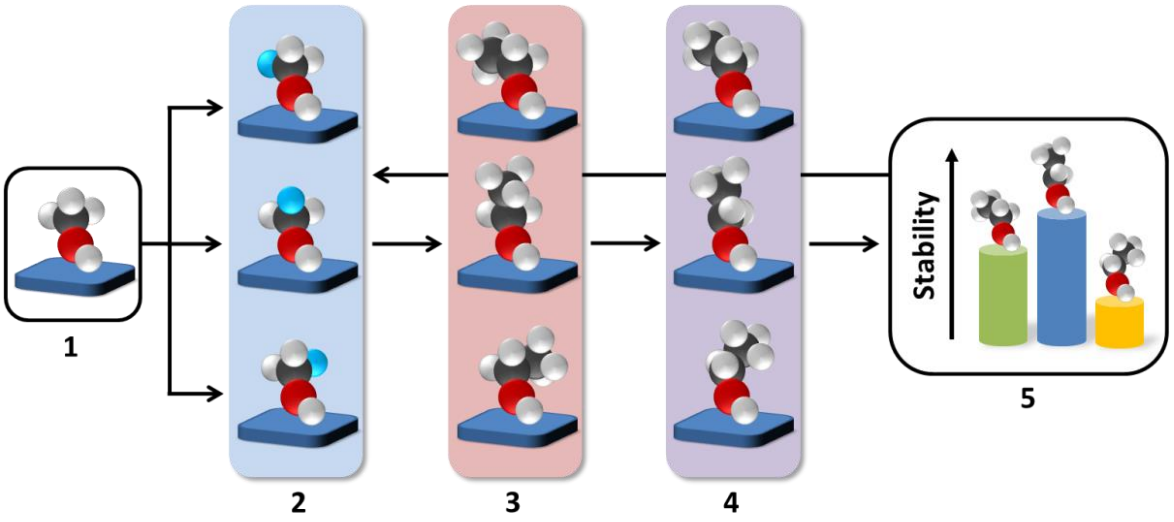

Figure S14. Illustration of the alcohol chain growth algorithm used in this work. C, O and H atoms are colour-coded grey, red and white, respectively. Boxes 1-5 are referred to in the above text.

5.6. Cyclohexane adsorption

The adsorption of cyclohexane at our optimised α-quartz surface has also been investigated. Saturation of the (0001) α-quartz surface was achieved at 0.5 ML surface coverage through a similar sampling scheme to that used for the investigation of methanol adsorption; the optimised configuration pertaining to the stable surface interaction identified is shown in Figure S15. The corresponding adsorption energy was calculated according to

$$E_{ads} = E_{mol+slab} - (2E_{mol} + 4E_{slab}). \quad \text{(S 12)}$$

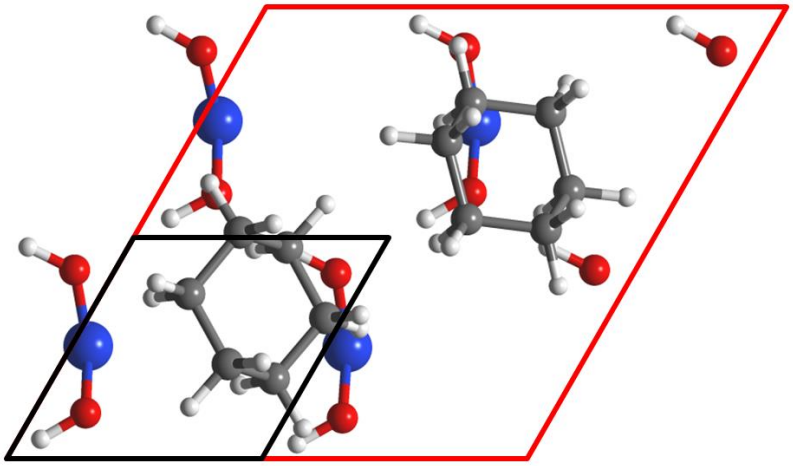

Figure S15. Top-down view of cyclohexane adsorbed at the (0001) α-quartz surface. Only surface atoms and adsorbates are shown for simplicity. The 1× 1 unit cell is indicated by black lines while the 2× 2 supercell used here is indicated in red. Si, C, O and H atoms are colour-coded blue, grey, red and white, respectively.

5.7. DFT summary

Table S6. Summary of PBE-D2 energies used in this work.

Adsorbate	E_{mol} / eV	E_{slab} / eV	$E_{mol+slab}$ / eV	E_{ads} / eV	E_{ads} / kJ mol^{-1}
1x1 α-quartz (0001) surface	-	-10792.7168	-	-	-
Cyclohexane	-1124.1868		-45419.5645	-0.3236	-31.22
Methanol	-655.6044	-	-11449.0270	-0.7058	-68.10
Ethanol	-843.1129	-	-11636.6163	-0.7866	-75.89
1-Propanol	-1030.4863	-	-11824.0675	-0.8644	-83.40
1-Butanol	-1217.8583	-	-12011.5530	-0.9780	-94.36

6. Supplementary references

1. Korb, J.-P. Multiscale nuclear magnetic relaxation dispersion of complex liquids in bulk and confinement. *Prog. Nucl. Magn. Reson. Spectrosc.* **104,** 12–55 (2018).
2. Brownstein, K. R. & Tarr, C. E. Spin-lattice relaxation in a system governed by diffusion. *J. Magn. Reson.* **26,** 17–24 (1977).
3. Aksnes, D. W., Førland, K. & Stöcker, M. 1H NMR relaxation and diffusion studies of cyclohexane and cyclopentane confined in MCM-41. *Microporous Mesoporous Mater.* **77,** 79–87 (2005).
4. Liu, G., Li, Y. & Jonas, J. Confined geometry effects on reorientational dynamics of molecular liquids in porous silica glasses. *J. Chem. Phys.* **95,** 6892–6901 (1991).
5. Delville, A. & Letellier, M. Structure and Dynamics of Simple Liquids in Heterogeneous Condition: An NMR Study of the Clay-Water Interface. *Langmuir* **11,** 1361–1367 (1995).
6. Bhatt, J. S., McDonald, P. J., Faux, D. A., Howlett, N. C. & Churakov, S. V. NMR relaxation parameters from molecular simulations of hydrated inorganic nanopores. *Int. J. Quantum Chem.* **114,** 1220–1228 (2014).
7. Weber, D., Mitchell, J., McGregor, J. & Gladden, L. F. Comparing Strengths of Surface Interactions for Reactants and Solvents in Porous Catalysts Using Two-Dimensional NMR Relaxation Correlations. *J. Phys. Chem. C* **113,** 6610–6615 (2009).
8. Levitt, M. H. *Spin Dynamics: Basics of Nuclear Magnetic Resonance*. (Wiley-Blackwell, 2008).
9. Stejskal, E. O. & Tanner, J. E. Spin Diffusion Measurements: Spin Echoes in the Presence of a Time-Dependent Field Gradient. *J. Chem. Phys.* **42,** 288–292 (1965).
10. Roy, D. *et al.* Nonpolar Adsorption at the Silica/Methanol Interface: Surface Mediated Polarity and Solvent Density across a Strongly Associating Solid/Liquid Boundary. *J. Phys. Chem. C* **117,** 27052–27061 (2013).
11. Wu, D., Guo, X., Sun, H. & Navrotsky, A. Energy Landscape of Water and Ethanol on Silica Surfaces. *J. Phys. Chem. C* **119,** 15428–15433 (2015).
12. Robinson, N., Gladden, L. F. & D'Agostino, C. Exploring catalyst passivation with NMR relaxation. *Faraday Discuss.* **204,** 439–452 (2017).
13. Wu, H., Gong, Q., Olson, D. H. & Li, J. Commensurate Adsorption of Hydrocarbons and Alcohols in Microporous Metal Organic Frameworks. *Chem. Rev.* **112,** 836–868 (2012).
14. Clark, S. J. *et al.* First principles methods using CASTEP. *Z. Für Krist.* **220,** 567–570 (2005).
15. Perdew, J. P., Burke, K. & Ernzerhof, M. Generalized Gradient Approximation Made Simple. *Phys. Rev. Lett.* **77,** 3865–3868 (1996).
16. Grimme, S. Semiempirical GGA-type density functional constructed with a long-range dispersion correction. *J. Comput. Chem.* **27,** 1787–1799 (2006).
17. Klimeš, J. & Michaelides, A. Perspective: Advances and challenges in treating van der Waals dispersion forces in density functional theory. *J. Chem. Phys.* **137,** 120901 (2012).
18. Gualtieri, A. F. Accuracy of XRPD QPA using the combined Rietveld–RIR method. *J. Appl. Crystallogr.* **33,** 267–278 (2000).
19. Monkhorst, H. J. & Pack, J. D. Special points for Brillouin-zone integrations. *Phys. Rev. B* **13,** 5188–5192 (1976).
20. Björkman, T., Gulans, A., Krasheninnikov, A. V. & Nieminen, R. M. Are we van der Waals ready? *J. Phys. Condens. Matter* **24,** 424218 (2012).
21. Levien, L., Prewitt, C. T. & Weidner, D. J. Structure and elastic properties of quartz at pressure. *Am. Mineral.* **65,** 920–930 (1980).

22. Goumans, T. P. M., Wander, A., Brown, W. A. & Catlow, C. R. A. Structure and stability of the (001) α-quartz surface. *Phys. Chem. Chem. Phys.* **9,** 2146–2152 (2007).
23. Rath, S. S., Sahoo, H., Das, B. & Mishra, B. K. Density functional calculations of amines on the (1 0 1) face of quartz. *Miner. Eng.* **69,** 57–64 (2014).
24. Abbasi, A., Nadimi, E., Plänitz, P. & Radehaus, C. Density functional study of the adsorption of aspirin on the hydroxylated (0 0 1) -quartz surface. *Surf. Sci.* **603,** 2502–2506 (2009).
25. de Leeuw, N. H., Higgins, F. M. & Parker, S. C. Modeling the Surface Structure and Stability of α-Quartz. *J. Phys. Chem. B* **103,** 1270–1277 (1999).
26. Musso, F., Sodupe, M., Corno, M. & Ugliengo, P. H-Bond Features of Fully Hydroxylated Surfaces of Crystalline Silica Polymorphs: A Periodic B3LYP Study. *J. Phys. Chem. C* **113,** 17876–17884 (2009).
27. Sun, W. & Ceder, G. Efficient creation and convergence of surface slabs. *Surf. Sci.* **617,** 53–59 (2013).
28. Boettger, J. C. Nonconvergence of surface energies obtained from thin-film calculations. *Phys. Rev. B* **49,** 16798–16800 (1994).
29. Fiorentini, V. & Methfessel, M. Extracting convergent surface energies from slab calculations. *J. Phys. Condens. Matter* **8,** 6525 (1996).
30. Rignanese, G.-M., Charlier, J.-C. & Gonze, X. First-principles molecular-dynamics investigation of the hydration mechanisms of the (0001) α-quartz surface. *Phys. Chem. Chem. Phys.* **6,** 1920–1925 (2004).
31. Han, J. W., James, J. N. & Sholl, D. S. First principles calculations of methylamine and methanol adsorption on hydroxylated quartz (0 0 0 1). *Surf. Sci.* **602,** 2478–2485 (2008).